

Subseasonal Predictability of Arctic Ocean Sea Ice Conditions: Bering Strait and Ekman-Driven Ocean Heat Transport

JED E. LENETSKY,^{a,b} BRUNO TREMBLAY,^a CHARLES BRUNETTE,^a AND GIANLUCA MENEGHELLO^c

^a *Department of Atmospheric and Oceanic Sciences, McGill University, Montreal, Quebec, Canada*

^b *National Snow and Ice Data Center, Cooperative Institute for Research in Environmental Sciences, University of Colorado Boulder, Boulder, Colorado*

^c *Department of Earth, Atmospheric and Planetary Sciences, Massachusetts Institute of Technology, Cambridge, Massachusetts*

(Manuscript received 13 July 2020, in final form 15 February 2021)

ABSTRACT: We use ocean observations and reanalyses to investigate the subseasonal predictability of summer and fall sea ice area (SIA) in the western Arctic Ocean associated with lateral ocean heat transport (OHT) through Bering Strait and vertical OHT along the Alaskan coastline from Ekman divergence and upwelling. Results show predictive skill of spring Bering Strait OHT anomalies in the Chukchi Sea and eastern East Siberian Sea for June and July SIA, followed by a sharp drop in predictive skill in August, September, and October and a resurgence of the correlation in November during freeze-up. Fall upwelling of Pacific Water along the Alaskan coastline—a mechanism that was proposed as a preconditioner for lower sea ice concentration (SIC) in the Beaufort Sea the following summer—shows minimal predictive strength on both local and regional scales for any months of the melt season. A statistical hindcast based on May Bering Strait OHT anomalies explains 77% of July Chukchi Sea SIA variance. Using OHT as a predictor of SIA anomalies in the Chukchi Sea improves hindcasts from the simple linear trend by 35% and predictions from spring sea ice thickness anomalies by 24%. This work highlights the importance of ocean heat anomalies for melt season sea ice prediction and provides observational evidence of subseasonal changes in forecast skill observed in model-based forecasts of the Chukchi Sea.

KEYWORDS: Sea ice; Heat budgets/fluxes; Seasonal forecasting; Statistical forecasting

1. Introduction

Skillful seasonal predictions of Arctic sea ice on a regional scale are important for the safe navigation of Arctic waters and for local indigenous communities who use sea ice for hunting, fishing, and recreational activities (Pearce et al. 2015; United States Navy 2014). State-of-the-art coupled ocean–ice–atmosphere models have been shown to provide skillful predictions of September pan-Arctic sea ice extent with lead times up to five months, both in seasonal forecast setups (Chevallier et al. 2013) and perfect model experiments (Bushuk et al. 2017; Tietsche et al. 2014; Day et al. 2014). The predictive skill of these seasonal sea ice forecasts is primarily attributable to the persistence of sea ice thickness (SIT) and ocean heat anomalies throughout the melt season (Guemas et al. 2016). For example, thinner ice in the late winter contributes to an earlier melt and increased surface ocean heat uptake in the summer. This signal is then amplified by the ice–albedo feedback and leads to a delayed freeze onset the following fall (Blanchard-Wrigglesworth et al. 2011, Bushuk et al. 2017).

The persistence of SIT and ocean heat anomalies have been used successfully to produce seasonal and regional forecasts of sea ice extent. In the Geophysical Fluid Dynamics Laboratory seasonal prediction system, regional forecasts of sea ice extent are skillful with 4–11 months of lead time (Bushuk et al. 2017). Skillful predictions with lead times as large as 11 months are primarily produced for winter ice conditions in the Atlantic sector, with skill derived from the initialization and persistence of ocean temperature anomalies (Bushuk et al. 2017). In the

Pacific sector, predictive skill for summer ice conditions is linked with SIT anomalies instead, and lead times of approximately four months do not differ significantly from those of observational studies (Brunette et al. 2019). Bushuk et al. (2017) find that reduced lead times for skillful forecasts in the Pacific sector compared to the Atlantic are due to less persistent sea ice extent and SIT anomalies, particularly in the spring and in line with declines in anomaly persistence seen in other model-based forecasts (Bonan et al. 2019; Blanchard-Wrigglesworth and Bushuk 2019).

The general consensus is that SIT anomalies are important for the seasonal prediction of summer ice conditions, and ocean heat anomalies for the prediction of fall and winter ice conditions (e.g., Bushuk et al. 2017; Guemas et al. 2016). Nonetheless, in specific regions of the Pacific sector, ocean heat transport (OHT) anomalies are important for sea ice predictability during the melt season. For example, Serreze et al. (2016) show that OHT through the Bering Strait is a skillful predictor of melt and freeze onset dates in the Chukchi Sea, with lead times of 1–2 months and average hindcast errors of 5 and 15 days, respectively. The skill of observation-based freeze onset forecasts from Serreze et al. (2016) match those produced by the CanSIPS forecasting system (Sigmond et al. 2016). For melt onset, however, CanSIPS predictions are not skillful because they rely instead on the persistence of spring sea ice concentration anomalies into the summer. The differences in predictability from observation- and model-based forecasts suggest that an improved understanding of the role of horizontal and vertical ocean heat transports in shaping summer ice conditions is still required.

Anomalously large Bering Strait OHTs in 2007 and 2011 led to an earlier opening of the pack ice, increased solar-driven sea

Corresponding author: Jed Lenetsky, jed.lenetsky@colorado.edu

DOI: 10.1175/JCLI-D-20-0544.1

© 2021 American Meteorological Society. For information regarding reuse of this content and general copyright information, consult the [AMS Copyright Policy](#) (www.ametsoc.org/PUBSReuseLicenses).

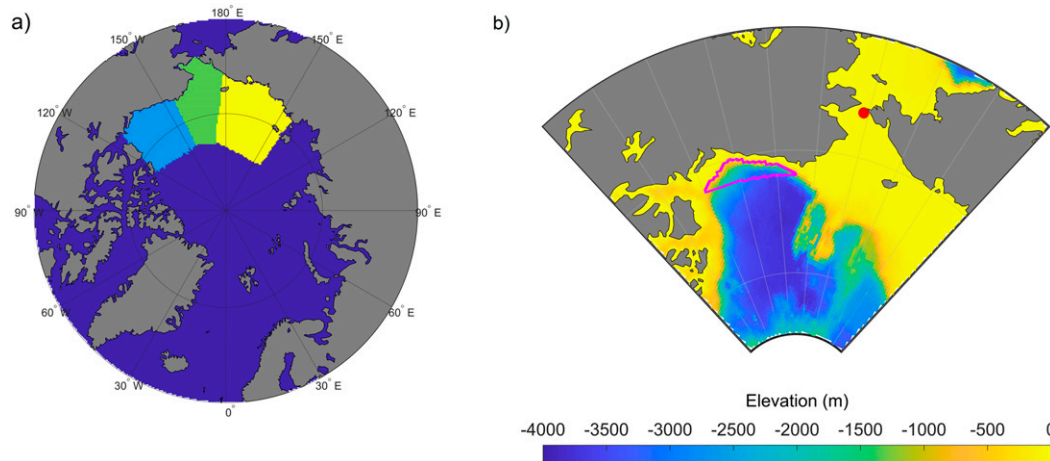


FIG. 1. (a) Arctic Ocean domain and definitions of the western Arctic peripheral seas, as per the NSIDC Arctic Ocean regional mask (Parkinson 2014): Beaufort Sea (blue), Chukchi Sea (green), and East Siberian Sea (yellow). The jagged edges defining each region gives an indication of the spatial resolution of the EASE-grid used in this study. (b) The bathymetry and definition of the Beaufort Sea continental slope region (magenta), defined between 130°–160°W and 70°–72°N, where ocean depth is greater than 300 m. The location of the A3 mooring marked in red.

ice melt, and rapid spring atmospheric warming (Woodgate et al. 2010; Woodgate 2018; Serreze et al. 2016). These relatively warm waters entering the broad shallow shelf of the Chukchi Sea (see Fig. 1) interact directly with the local sea ice cover and can effectively reduce sea ice thickness before mixing with cooler waters from the central Arctic basin (Pickart et al. 2016; Auclair and Tremblay 2018). This early melt increases the area of open water that is exposed to direct solar radiation, further warming the ocean mixed layer and amplifying sea ice loss (i.e., the ice-albedo feedback; Perovich et al. 2007; Woodgate et al. 2010). Bering Strait OHT variability is primarily driven by remote zonal winds anomalies in the East Siberian Sea, which can set up sea surface height gradient anomalies between the North Pacific and Arctic Oceans, increasing the volumetric transport of Pacific Water into the Arctic (Serreze et al. 2019; Peralta-Ferriz and Woodgate 2017; Danielson et al. 2014). Pacific Water temperatures and local northerly (along-strait) winds can amplify or diminish the transport of ocean heat into the Arctic Ocean (Serreze et al. 2019; Woodgate 2018).

Warm water of Pacific origin exits the Chukchi Sea via three common pathways: the Harold Canyon on the Western Continental Shelf, the Barrow Canyon over the Eastern Shelf, and a central branch over the Harold Shoal (Pickart et al. 2016). In the summer and fall, the central and eastern branches carry the majority of Pacific Water and heat into the Arctic Ocean interior, which together form the Beaufort Shelfbreak jet, traveling eastward along the Alaskan–Beaufort Sea coastline between 50 and 150 m below the surface (Steele et al. 2004; Gong and Pickart 2015; Foukal et al. 2019; Lin et al. 2016). Along the Alaskan coastline, semipermanent zonal winds associated with the Beaufort high transport sea ice westward (Yang 2006; Tandon et al. 2018). The east–west sea ice stress results in local Ekman offshore transport into the Beaufort Sea

interior, leading to surface convergence and downwelling in the Canada Basin interior and upwelling along the Alaskan coastline (Yang 2006; Meneghello et al. 2018b; Lin et al. 2019; Timmermans et al. 2014). These Ekman dynamics are further complicated by the presence of geostrophic currents, which, along with extensive sea ice cover, can either reverse the ice-stress curl and lead to intense periods of upwelling in the Canada Basin interior in the fall and winter or accelerate the ice-stress curl along the Beaufort Sea continental slope (Meneghello et al. 2018a,b). It has been hypothesized that vertical Ekman pumping along the Alaskan coastline could reduce winter sea ice growth and act as a thermodynamic preconditioning mechanism for reduced sea ice extents in the Beaufort Sea (Dmitrenko et al. 2018; Okkonen et al. 2009; Pickart et al. 2009; Babb et al. 2016). To test this hypothesis, we also include an analysis of vertical ocean heat transport along the Alaskan coastline and its impact on subseasonal sea ice predictability in the western Arctic.

The goal of this paper is to understand the persistence of ocean heat anomalies from horizontal and vertical OHTs in the melt season, and to bridge the gap in sea ice predictability between the melt onset and freeze onset reported by Serreze et al. (2016). In addition, we develop a statistical hindcast model for the seasonal prediction of sea ice area (SIA). We show that oceanic heat transport through Bering Strait is a skillful predictor for sea ice concentration (SIC) in the Chukchi Sea and eastern East Siberian Sea in June and July but loses strength as a predictor in late summer, and that vertical ocean heat transport by Ekman pumping along the Alaskan coastline has little predictive skill at seasonal time scales.

The paper is structured as follows. Section 2 outlines the datasets used in this study. We describe the temporal and spatial variance of SIC and SIA predictability associated with the Bering Strait OHT in section 3a, and Ekman pumping in

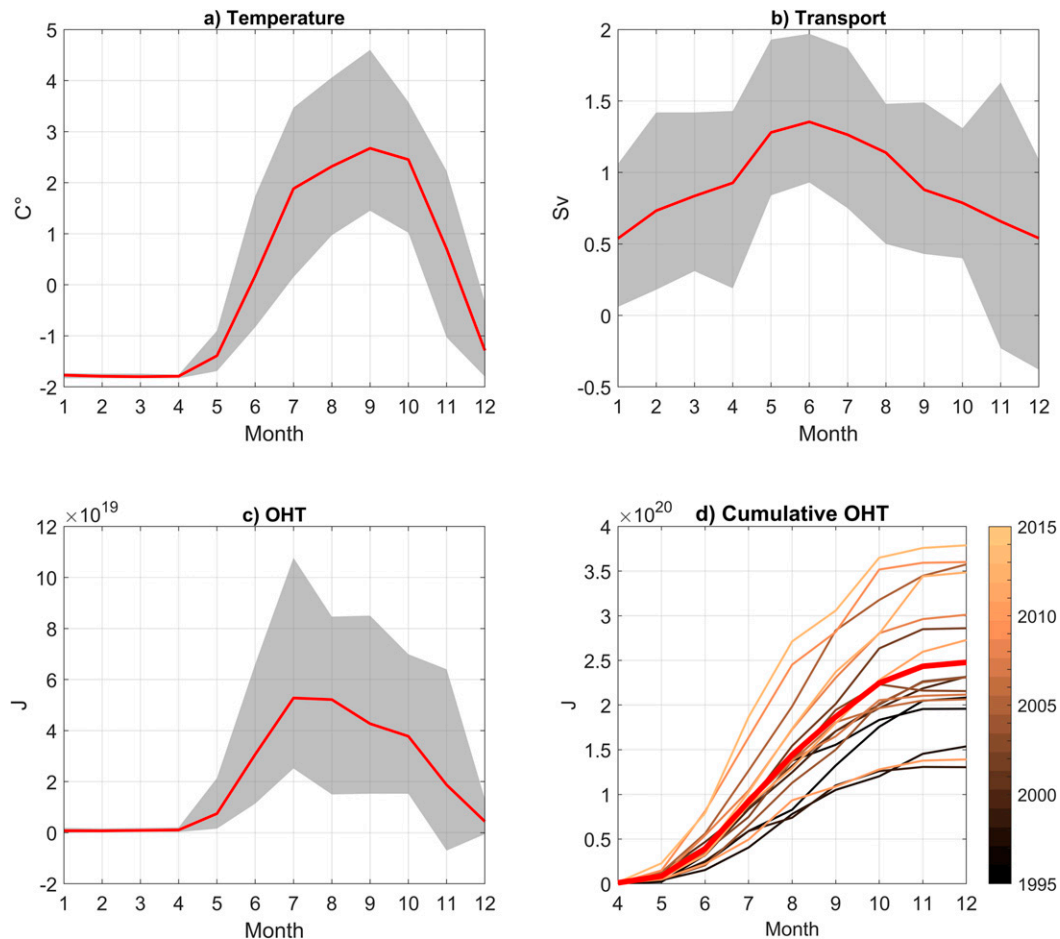


FIG. 2. Variability in the ocean heat transport (OHT) through the Bering Strait and its components: (a) temperature, (b) volume transport, (c) monthly mean noncumulative OHT, and (d) yearly cumulative OHT from April through month m . The red line indicates the 1998–2015 mean, and the gray shading indicates the total range.

the Beaufort Sea in section 3b. We also propose physical mechanisms responsible for the observed differences in SIC predictability from the Bering Strait OHT and Ekman pumping along the Alaskan coastline. Finally, we present a hindcast model of SIA in Chukchi Sea based on May Bering Strait OHT anomalies and compare the forecast skill of this model with that of other models using different predictors (section 3c). The main conclusions from this study are summarized in section 4.

2. Data

The monthly mean Bering Strait OHT time series is derived from hourly, near-bottom temperature and transport observations from 1998 to 2015 from the A3 mooring deployed 35 km north of the Bering Strait at a depth of 57 m (see Figs. 1 and 2; Woodgate 2018; Woodgate et al. 2015). This mooring was chosen based on the consistency and quality of the observational record, and its location at the outlet of the Bering Strait limits the influence of in-strait variations of velocity and temperature (Woodgate 2018). Moorings A1 and A2, which

are located in the Russian and U.S. regions of the strait, respectively, have temporally inconsistent and uncorrected records, and do not provide representative OHT estimates for the entire strait (Woodgate 2018). Data from the A3 mooring, however, do not include the nonnegligible contribution of the Alaskan Coastal Current (Woodgate 2018). For the total Bering Strait OHT, A3 recordings should in principle be supplemented with data from the A4 mooring, located just off the Alaskan Coast since 2001. Due to the limited length of the A4 time series, we only include data from the A3 mooring in the OHT calculations, resulting in the underestimation of the Bering Strait OHT by approximately 25%. Nonetheless, in Woodgate (2018), temperature and velocity measurements from the A3 and A4 mooring are found to be strongly and significantly correlated ($r > 0.75$; see Woodgate 2018, p. 129, Table 3 therein) and show almost identical trends (see Woodgate 2018, p. 127, Table 1 therein). Thus, the A3 mooring is considered a representative record of Bering Strait OHT variability (Serreze et al. 2016; Woodgate 2018).

The cumulative monthly mean Bering Strait OHT (J) from April ($m = 4$) to month M can be written as

$$\text{OHT}_M = k\rho_w C_{pw} \sum_{m=4}^M (T_{wm} - T_w^{\text{ref}}) V_m P_m, \quad (1)$$

where ρ_w is the density of ocean water ($= 1023 \text{ kg m}^{-3}$), C_{pw} is the specific heat of ocean water ($= 3900 \text{ J kg}^{-1} \text{ K}^{-1}$), T_{wm} is the monthly mean observed near-bottom temperature of water in the Bering Strait for month m (considered representative of the largely barotropic water column), T_w^{ref} is the reference freezing point temperature of ocean water for the annual mean Bering Strait salinity of 32.5 psu (-1.9°C), V_m (Sv ; $1 \text{ Sv} \equiv 10^6 \text{ m}^3 \text{ s}^{-1}$) is the monthly mean volumetric water transport through the Bering Strait for month m , P_m is the total length of the each month m (s), and k ($= 10^6 \text{ m}^3 \text{ s}^{-1} \text{ Sv}^{-1}$) is the conversion factor from Sverdrups to $\text{m}^3 \text{ s}^{-1}$.

The OHT is calculated relative to a reference salinity-dependent freezing temperature, at which Bering Strait waters leave the Arctic Ocean through the Fram Strait and Canadian Arctic Archipelago. This allows for the estimation of how much heat from Pacific Water has been transferred to the Arctic Ocean throughout its transit (Woodgate 2018). OHT estimates are robust to the exact choice of reference salinity, within a 5% error (Woodgate 2018). In this time series, the month of June 1999 was missing and was filled with the average of the May and July OHT of the same year. In the following, monthly correlations are performed using the cumulative OHT of a given year beginning in April, as it is the first month in the year where OHT is nonzero as per our definition (see Fig. 2).

We use SIC from the monthly NOAA/NSIDC Climate Data Record (CDR) of passive microwave sea ice concentration, from January 1979 to December 2018 (Meier et al. 2017). The dataset is based on brightness temperatures from a variety of passive microwave sensors to differentiate between sea ice and open water (Peng et al. 2013). Brightness temperatures are converted to sea ice concentration measurements using a rule-based classification (CDR algorithm) that relies on the highest output of two different proven algorithms, NASA Team and NASA Bootstrap (Peng et al. 2013). We interpolate the SIC data from a polar stereographic grid to the Equal-Area Scalable Earth Grid (EASE-Grid) with a resolution of $25 \text{ km} \times 25 \text{ km}$. SIA is assessed as the sum of all SIC grid cells in the regional domain, multiplied by grid cell area (625 km^2).

We use the total Beaufort Gyre Ekman pumping velocity from 2003 to 2014, from Meneghello et al. (2018b). Ekman pumping velocity is estimated using bulk formulas and combining (i) SIC from *Nimbus-7* SMMR and DMSP SSM/I-SSMIS passive microwave data, version 1 (Cavalieri et al. 1996); (ii) sea ice velocity from the Polar Pathfinder daily 25-km EASE-Grid sea ice motion vectors, version 3 (Tschudi et al. 2016); (iii) geostrophic currents computed from dynamic ocean topography (Armitage et al. 2016, 2017); and (iv) 10-m wind from the NCEP-NCAR Reanalysis 1 (Kalnay et al. 1996). The passive microwave-derived SIC is used to account for the differential stresses of the ice-covered versus open ocean at the sub-gridcell resolution. This dataset is notable as it includes the role of geostrophic currents, which can modify Ekman pumping rates and direction (Meneghello et al. 2018b). The length of the

Ekman pumping velocity time series is limited by the discontinuation of the Envisat satellite in 2014, which is used by Armitage et al. (2017) to calculate geostrophic currents. We present results for averaged fall (October–December) Ekman velocities along the Alaskan continental shelf where upwelling is largest, defined between 130° – 160°W and 70° – 72°N , and where ocean depth is greater than 300 m, as shown in Fig. 1b (Meneghello et al. 2018b).

To compare the predictive strength of spring ice thickness anomalies and Bering Strait OHT anomalies, we use the mean May SIT calculated from the Pan-Arctic Ice Ocean Modeling and Assimilation System (PIOMAS) monthly mean data from 1979 to 2015 (Schweiger et al. 2011; Zhang and Rothrock 2003). PIOMAS is a coupled ice–ocean model that assimilates sea ice concentrations and sea surface temperatures in order to produce SIT fields (Schweiger et al. 2011). PIOMAS ice thickness retrievals generally agree well with observational data from ICESAT ($< 0.1\text{-m}$ mean difference) with the exception of coastal areas in the Chukchi and Beaufort Seas, where ice is thinner compared to ICESAT, and north of Greenland and the Canadian Arctic Archipelago, where ice is thicker than ICESAT observations (Schweiger et al. 2011). Despite these biases, PIOMAS SIT retrievals reasonably capture monthly and inter-annual variability in ice thickness, and warrants its use in this study. For consistency across datasets, we interpolate PIOMAS SIT onto the EASE-grid.

To bolster our observational results, we also perform complimentary analyses using the Estimating the Circulation and Climate of the Ocean (ECCO) reanalysis version 5 from 1992 to 2017 (ECCO Consortium et al. 2020a,b). The ECCO reanalysis uses the MIT general circulation model initialized using atmospheric fields from the ERA-Interim reanalysis, and all available satellite, mooring, and ARGO float data to calculate the ocean and sea ice state at a daily resolution (Forget et al. 2015). We use ECCO estimates at a monthly, $1/4^\circ$ horizontal, and 10-m (near the surface) vertical resolution. Bering Strait OHT is calculated from zonally and vertically integrating average meridional velocities (V_m) and temperatures (T_{wm}) across the entire strait (64° – 67°N , 168° – 179°W ; 5–60-m depth), and applied to Eq. (1) in the text. Thus, ECCO OHTs differ from OHTs from the A3 mooring, which are calculated from monthly mean water properties at a singular location in the strait. The correlation between OHT detrended anomalies from the A3 mooring and ECCO is 0.97. This is in accord with the findings of Woodgate (2018), who show that the A3 mooring captures water properties that are representative of the Bering Strait as whole. Beaufort Sea Ekman velocities are calculated from 20-m ECCO vertical velocities, the approximate Ekman layer depth (Yang 2006), averaged across the Alaskan coastal region outlined in Fig. 1. Correlations between observed and ECCO Ekman pumping velocities are significantly correlated ($r = 0.50$) but show less agreement than Bering Strait OHT estimates. This discrepancy is likely due to disagreements between NCEP-NCAR and ERA-Interim atmospheric forcings over the relatively small Alaskan coastal region. When compared over larger regions, such as the entire Beaufort Sea, Ekman velocities show closer agreement ($r = 0.72$).

TABLE 1. Correlations between monthly mean detrended Bering Strait OHT anomalies, temperature anomalies, and transport anomalies and Chukchi Sea SIA anomalies for the 1998–2015 time period. Significant correlations ($p < 0.05$) are shown in bold.

	May SIA	June	July	August	September	October	November	December
OHT								
May	-0.65	-0.77	-0.74	-0.36	-0.17	-0.21	-0.48	-0.01
June	—	-0.67	-0.71	-0.44	-0.32	-0.30	-0.42	0.04
July	—	—	-0.70	-0.38	-0.25	-0.24	-0.43	-0.05
August	—	—	—	-0.38	-0.28	0.31	-0.51	-0.11
September	—	—	—	—	-0.29	-0.39	-0.65	-0.32
Temperature								
May	-0.58	-0.78	-0.77	-0.42	-0.21	-0.28	-0.51	-0.21
June	—	-0.76	-0.79	-0.37	-0.23	-0.19	-0.37	-0.02
July	—	—	-0.70	-0.20	-0.14	-0.21	-0.66	-0.29
August	—	—	—	-0.43	-0.31	-0.42	-0.63	-0.09
September	—	—	—	—	0.00	-0.26	-0.62	-0.16
Transport								
May	-0.55	-0.29	-0.29	-0.31	-0.24	-0.12	-0.19	0.04
June	—	-0.27	-0.20	-0.42	-0.41	-0.40	-0.25	0.13
July	—	—	-0.26	-0.25	-0.11	-0.09	0.00	0.07
August	—	—	—	-0.06	-0.12	-0.18	-0.21	-0.24
September	—	—	—	—	-0.13	-0.24	-0.44	-0.60

We calculate anomalies of SIC, SIA, OHT, SIT, and Ekman velocities by linearly detrending each time series over matching time periods. The correlations presented in the results section are taken between anomalies of SIC/SIA and OHT/Ekman velocity and are considered statistically significant at the 95% significance level ($p < 0.05$), unless otherwise mentioned.

3. Results and discussion

a. Variability in SIC and ocean heat transport

Monthly mean cumulative Bering Strait May OHT anomalies are strongly correlated with SIA anomalies in the Chukchi Sea for the month of May ($r = -0.65$), June ($r = -0.77$) and July ($r = -0.74$), with a sharp decline in covariability in August, despite a decorrelation time scale in the noncumulative May Bering Sea OHT anomaly of 3 months (see Table 1 and Fig. 3). One factor that may be at play in the decline in correlation beyond July is the (unpredictable) dynamical loss of ice area in late summer and the fact that the sea ice edge is moving farther away from the mouth of the Bering Strait and continental shelf where ocean heat is interacting directly with the sea ice cover. Note however that July coastal divergence in the Chukchi Sea can skillfully predict September sea ice extent in the Chukchi Sea, suggesting that both dynamical preconditioning (thinner ice cover in the Chukchi Sea from late winter coastal divergence) and thermodynamical (Bering Strait OHT) processes may be important for seasonal prediction in this area (Kim et al. 2020, manuscript submitted to *J. Climate*). We also see a reemergence of sea ice predictability in the fall: the May Bering Strait OHT is correlated with monthly Chukchi SIA anomaly in November with a coefficient of $r = -0.48$ (see Table 1 and Fig. 4). Weekly correlations, while nonsignificant in November, still show a broader pattern of fall resurgence. These findings are in agreement with the observational studies of Serreze et al. (2016), as well as the model-based study of Bushuk

et al. (2017), who show that November Chukchi SIA is predictable from as early as May with 7 months of lead time. This suggests that improved forecasts of Chukchi SIA in early summer and fall (near melt and freeze onset) may be possible with a proper representation of OHT through the Bering Strait in coupled and forced ice-ocean models. The Bering Strait OHT is not significantly correlated with SIA in any other seas throughout the melt season.

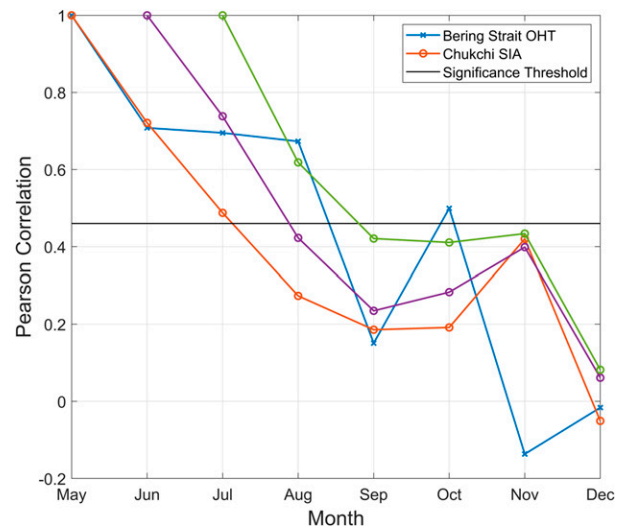


FIG. 3. Autocorrelation of detrended noncumulative Bering Strait OHT anomalies (blue) and detrended Chukchi Sea SIA anomalies for May (red), June (purple), and July (green). The 95% statistical significance threshold for 17 degrees of freedom ($r = 0.46$) is shown in black. The decorrelation time scale for Bering Strait OHT and SIA are approximately 3 and 2 months, respectively.

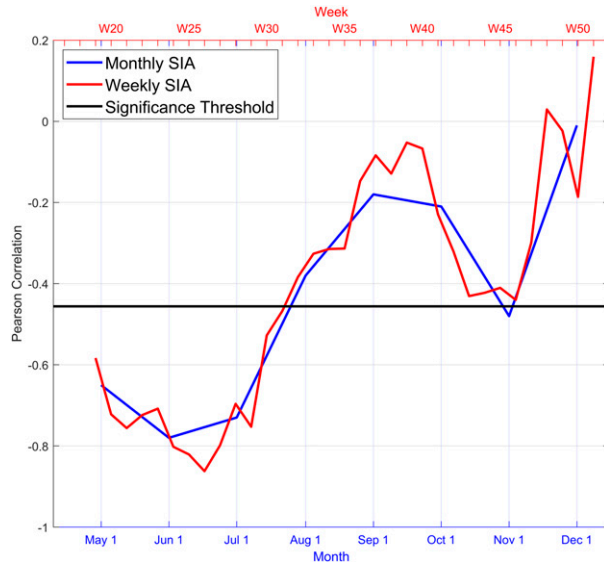


FIG. 4. Correlations between detrended cumulative May Bering Strait OHT anomalies, and detrended May–December Chukchi SIA anomalies (monthly: blue; weekly: red). 95% statistical significance threshold for 17 degrees of freedom ($r = 0.46$) is shown in black.

To further discern a causal link between OHT anomalies and sea ice conditions in the Chukchi Sea, we decompose the OHT signal into its temperature and volume transport components and relate them to SIA anomalies (see Table 1). Comparisons of correlation strength between Bering Strait temperature and volume transport anomalies demonstrate that predictive skill from OHT in May, June, July, and November is primarily derived from ocean temperature variability. Correlations between velocity and SIA anomalies in the above months are only significant in May. Furthermore, correlations between Bering Strait temperature and OHT anomalies show a seasonal cycle in which fall, summer, and winter OHT variability is primarily determined by variability in volume transports, whereas spring OHT variability is primarily determined by water temperature variability (see Fig. 5). The importance of water temperatures peak in May and June, with May water temperatures explaining 89% of May OHT variability. Thus, the months in which OHT exhibits the strongest predictive skill (May and June) are the same months in which the importance of Bering Strait temperatures outweighs the importance of volume transports. These findings confirm that Chukchi SIA predictability from OHT is due to direct interactions between ocean temperature anomalies and sea ice cover, and not due to covariations between atmospheric circulation patterns (which determine volume transport anomalies) and sea ice conditions in the Chukchi Sea.

We now look at the spatial pattern of the correlations between OHT and SIC as a test of the proposed link between Bering Strait heat transport and western Arctic SIA variability (see Fig. 6). Bering Strait OHT has the largest influence on Arctic SIC on the continental shelf where the ocean is shallow and ocean heat entering the Arctic is in direct contact with sea ice (Pickart et al. 2016; Auclair and Tremblay 2018; Lu et al. 2020). Furthermore, Pacific Water is largely constrained to the



FIG. 5. Explained variance of detrended Bering Strait temperature (black) and volume transport (red) anomalies, for detrended Bering Strait OHT anomalies.

Chukchi and Beaufort Sea continental slopes, limiting the penetration of Pacific Water into the Canada Basin (von Appen and Pickart 2012; Spall et al. 2018). For the Pacific Water that does enter the Canada Basin interior, mechanisms for vertical ocean heat transport over the deeper ocean, such as Ekman pumping associated with positive ice–ocean surface stress curl and turbulent mixing, are less effective at bringing heat of Pacific origin to the surface mixed layer compared to the direct interactions over the continental shelf (Timmermans et al. 2014; Toole et al. 2010). These processes act to limit the influence of the Bering Strait OHT to the western Arctic Ocean’s margins.

The influence of OHT-induced melt is limited to the Bering Strait in May, and then, as Pacific Water circulates throughout the Chukchi Sea, extends offshore in June, and covers the entire Chukchi Sea as well as large areas of the East Siberian Sea (ESS) in July. The eastern half of the ESS is dynamically more similar to the Chukchi Sea than the western half when it comes to subseasonal predictability of sea ice conditions. For instance, May Bering Strait OHT is also correlated with SIC in the eastern ESS in July with a sharp loss of predictive strength in August and September. Bering Strait OHT anomalies, however, are not correlated with June SIC anomalies in the western ESS because it is farther away from the mouth of the strait and the advective time scale for OHT to reach this part of ESS is approximately one month. Thus, the strongly, negatively correlated portions in the eastern part of the East Siberian Sea are offset by nonsignificant correlations in the western regions of the sea ($r = 0.44$, $p = 0.07$). Additionally, in July, we also observe an extension of larger correlations (not significant) over the Canada Basin and north of the Canadian Arctic Archipelago in accord with known pathways of Pacific Water entering the western Arctic (Jahn et al. 2010).

In August, September, and October, regions of high correlation are smaller and highly fragmented, in line with the loss of

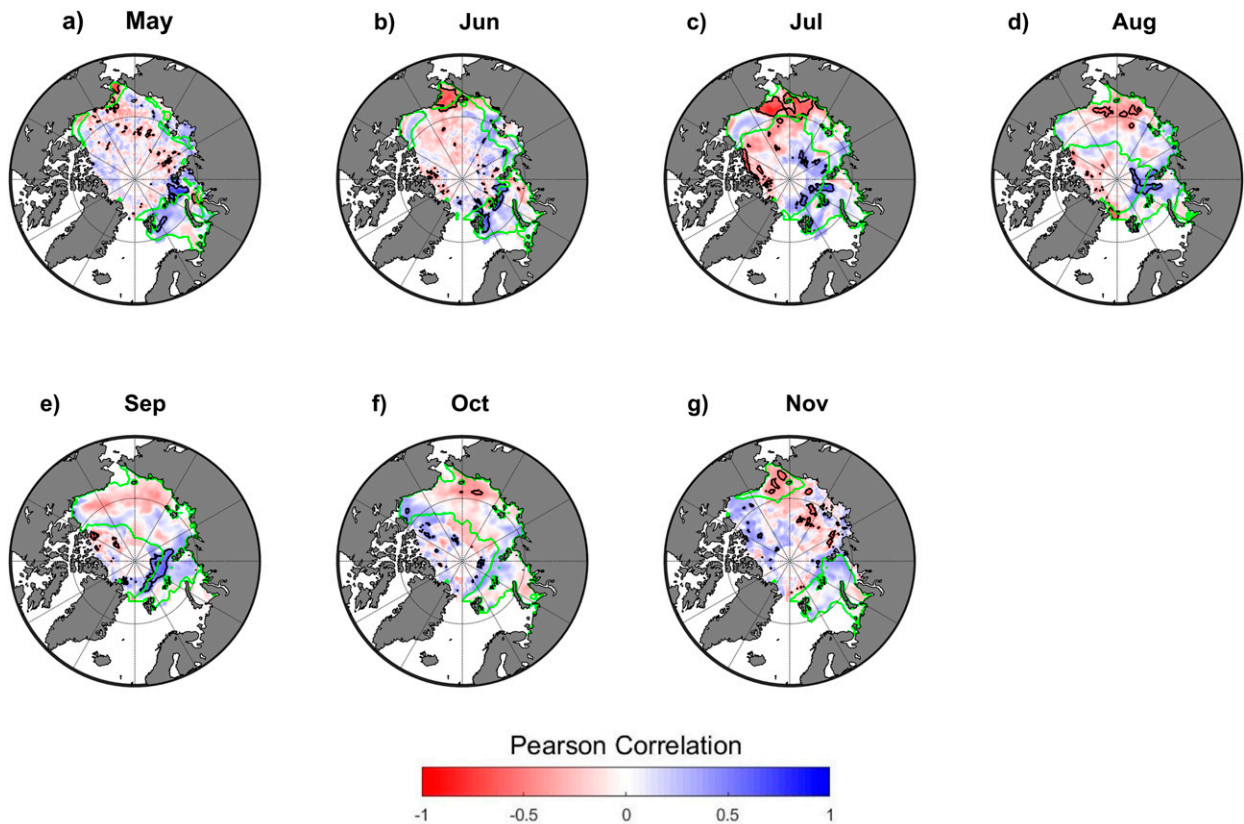


FIG. 6. Correlations between detrended cumulative observed May Bering Strait OHT anomalies and detrended monthly mean SIC anomalies for the month of (a) May, (b) June, (c) July, (d) August, (e) September, (f) October, and (g) November. Significant correlations (95% significance level) are outlined in black, and regions where the interannual variability in monthly SIC is larger than 10% are outlined in green.

correlation reported above (see Table 1). We associate the loss of predictive skill in late summer with summer stratification over the continental shelf, the dynamical loss of sea ice, and the ice-albedo feedback. Idealized model experiments over the Chukchi Sea continental shelf have shown that despite the Bering Strait OHT providing heat for 70% of sea ice melt in the spring marginal ice zone, by August and September an increasingly thick layer of meltwater sits atop the Pacific Water layer, creating stable stratification and significantly reducing interactions between sea ice and Pacific Water heat (Lu et al. 2020). The timing of this fresh surface layer and reduced OHT influence also corresponds to a thinner and more fragmented summer ice pack in which winds exert greater control over the sea ice cover. A thinner ice pack is more mobile, and thus more responsive to surface winds and summer storm activity (Lei et al. 2020). Furthermore, summer synoptic-scale cyclones have complex thermodynamic effects on sea ice, slowing melt by cooling temperatures (Schreiber and Serreze 2020) while also increasing bottom melt by generating waves that promote increased upwelling of ocean heat to the surface (Zhang et al. 2013). Additionally, as a fractured ice pack exposes more open water to solar heating, the ice-albedo feedback becomes a dominant mechanism of further ice melt (Perovich et al. 2007).

The above processes both reduce the relative influence of the Bering Strait OHT and drive the variability of summer SIA in the Chukchi Sea, overriding most of the early-season signature from ocean heat, and are not predictable at seasonal time scales (Serreze et al. 2016). We conclude that the loss of late summer sea ice predictability is due to the above processes, rather than the Chukchi Sea becoming ice free. From 1998 to 2015, the September Chukchi Sea ice cover exhibits sizeable variability but has only twice become ice-free, in 2007 and 2012.

The loss of predictive skill from Bering Strait OHT for late summer SIA in the Chukchi Sea is in accord with modeling results from Bushuk et al. (2017) using a fully coupled global climate model. As such, August through October represent a predictive “gap” in the Chukchi Sea. This gap in predictive skill occurs when ice melts—isolating the surface waters from temperature anomalies at depth—and reemerges in the fall during freeze up when the seasonal halocline is eroded and ocean heat is ventilated at the surface, affecting the freeze onset date (Bushuk et al. 2017; Blanchard-Wrigglesworth et al. 2017). In November, we see small areas with negative correlations on the Chukchi Sea continental shelf, resulting in sea ice predictability at the regional scale.

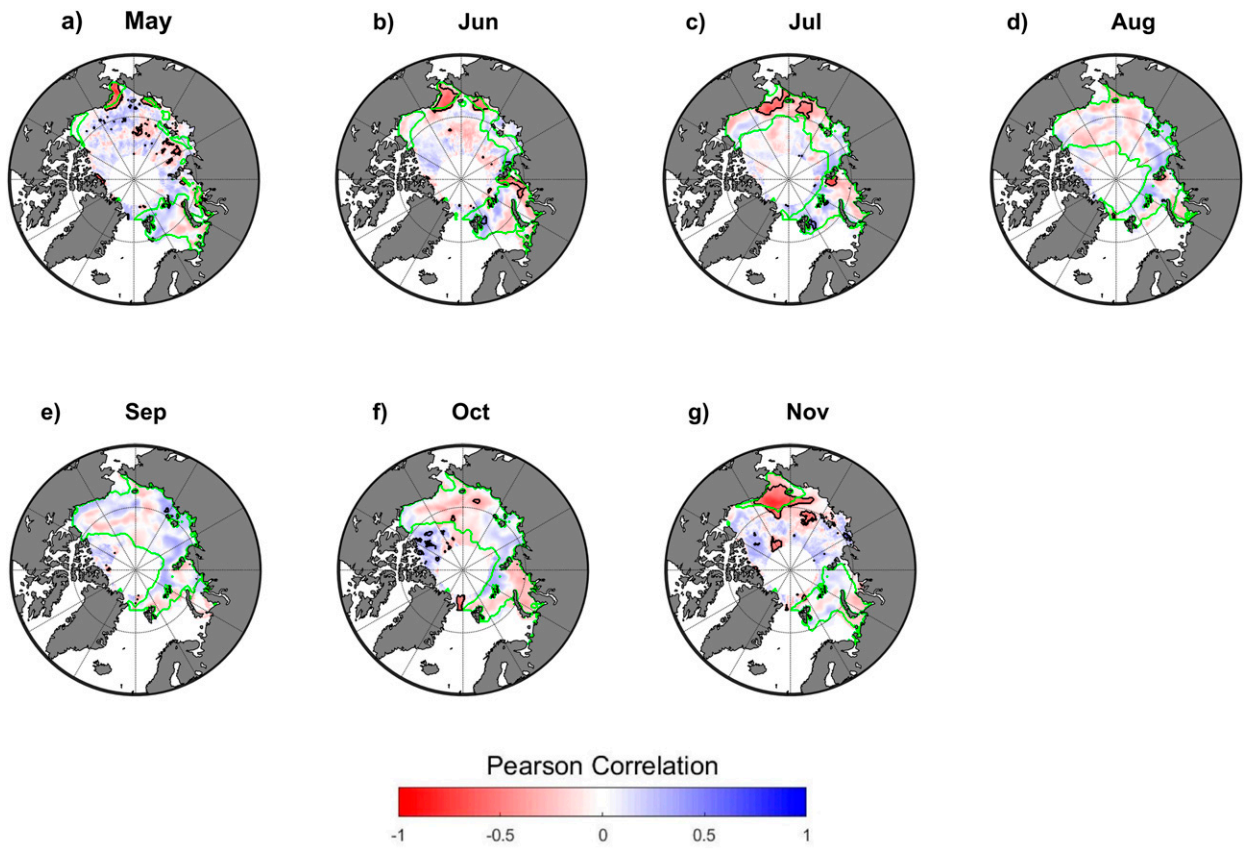


FIG. 7. Correlations between detrended cumulative ECCO May Bering Strait OHT anomalies and detrended monthly mean SIC anomalies for the month of (a) May, (b) June, (c) July, (d) August, (e) September, (f) October, and (g) November. Significant correlations (95% significance level) are outlined in black, and regions where the interannual variability in monthly SIC is larger than 10% are outlined in green.

Interestingly, positive correlations between cumulative Bering Strait OHT and SIC anomalies are observed in the Atlantic sector for all months from May to September. Regions of strong positive signal is observed in the northern regions of the Barents and Kara Seas ($r = 0.6$; see Figs. 6a–e). These remote regions of covariability are akin to those reported in Auclair and Tremblay (2018) in the Community Earth System Model Large Ensemble, and appear to be caused by atmospheric circulation patterns that drive anomalous sea ice drift and covariability between Pacific and Atlantic volume transports. For instance, Boer et al. (2018) show in model simulations that volume transports through the Bering Strait and the Fram Strait/Barents Sea Opening (BSO) are strongly anticorrelated. This relationship is due to both conservation of mass via oceanic sea surface height adjustment, and large-scale atmospheric conditions (Timmermans and Marshall 2020; Stigebrandt 1981). They found that large-scale atmospheric circulation patterns (e.g., linked with the Arctic Oscillation and Aleutian low) result in increased pressure head and volume transport through the Bering Strait, in accord with results from Danielson et al. (2014); Serreze et al. (2019). At the same time, these circulation patterns generate northerly and northwesterly winds in the Barents and Kara Seas, which in turn reduce

northward volume transport through the Fram Strait and BSO while advecting sea ice into the region. Thus, our results provide observational evidence that increased volume (and heat) transport of Pacific Water coincides with increased ice concentrations in the Atlantic sector, which we attribute to both sea ice advection into the region and limited volume transport (and heat) into the Arctic from the Atlantic Ocean. As a result, these mechanisms can increase SIC in the Atlantic sector of the Arctic and become a source of predictability for the entire melt season.

The same spatial and temporal patterns are seen in correlation maps between ECCO OHT and SIC from 1992 to 2017 (see Fig. 7). May cumulative ECCO OHT anomalies are correlated with SIC anomalies over the Chukchi Sea continental shelf from May through July, with a sharp drop in predictive skill from August through October, and a return of predictive skill in November along the continental shelf. However, some key differences exist, namely reduced positive correlations in the Atlantic sector of the Arctic Ocean and an even more pronounced loss of predictive skill in the Pacific sector in August. Despite these discrepancies, which highlight uncertainties in both the mooring and ECCO OHT time series, the two datasets agree and lend additional confidence to our primary findings that 1) predictive skill from the Bering Strait

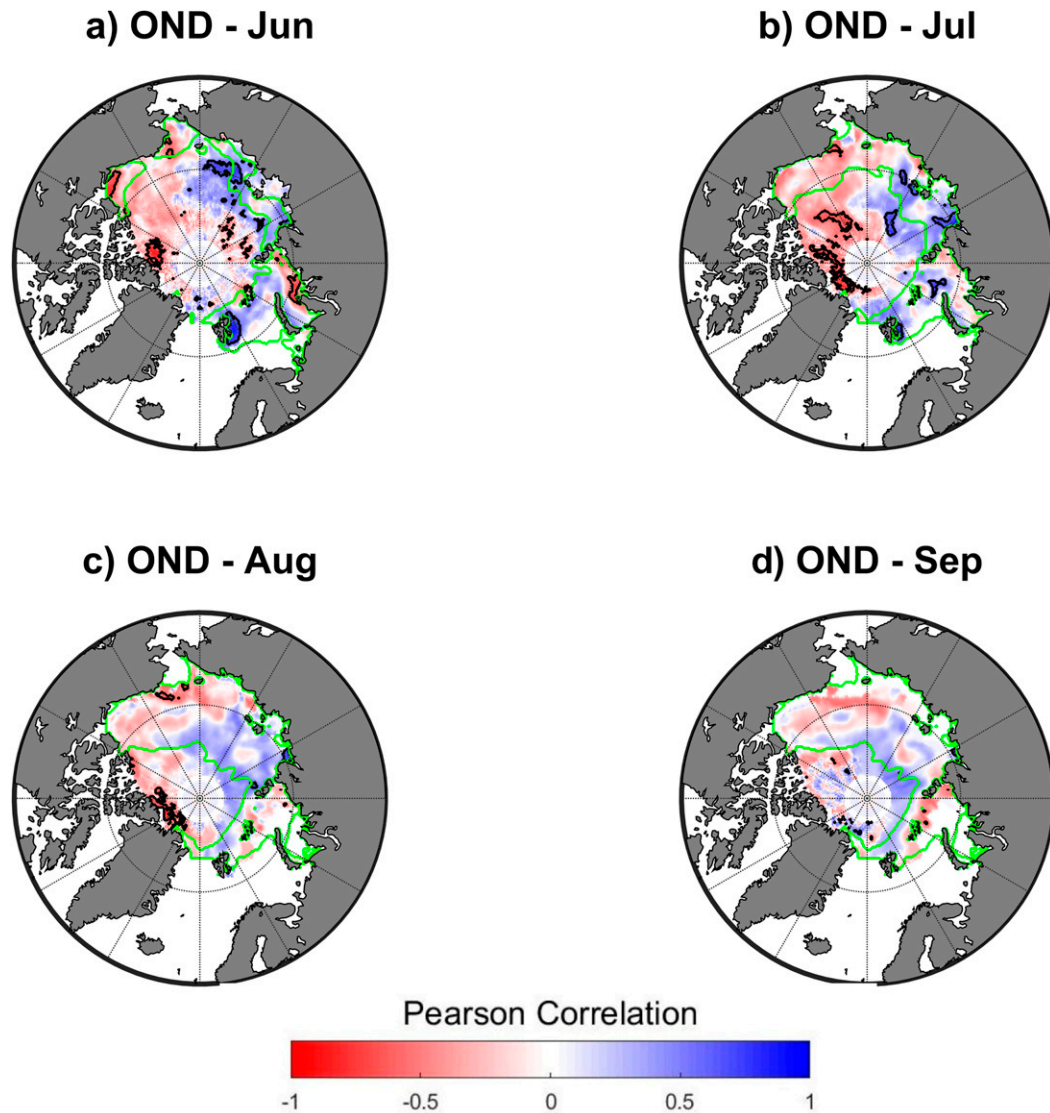


FIG. 8. Correlations between detrended observed October–December mean Ekman pumping velocity anomalies along the Alaskan coastline (magenta box in Fig. 1) and detrended (a) June, (b) July, (c) August, and (d) September sea ice concentration anomalies. Significant correlations (95%) are outlined in black, and regions where the interannual variability in monthly SIC varies by more than 10% are outlined in green.

OHT is highest for sea ice over the continental shelves of the Chukchi Sea and the eastern ESS, and 2) there is strong sub-seasonal variability in the strength of this predictive skill.

b. Variability in SIC associated with Ekman pumping

Correlations between mean October–December Ekman pumping velocity anomalies from both observations and the ECCO reanalysis show a weak relationship between upwelled ocean heat along the Alaskan coastline and SIC. October–December mean Ekman pumping velocity anomalies derived from observations are (weakly) negatively correlated with SIC anomalies in the Beaufort and Kara Seas and (weakly) positively correlated in the East Siberian and Laptev Seas from June through September (see Fig. 8). We argue that this triple

pattern is associated with coupled variability between SIC and large-scale atmospheric circulation patterns rather than upwelling of ocean heat [e.g., see Fig. 5 from Armstrong et al. (2003)]. Fall upwelling along the Alaskan coastline is associated with anticyclonic wind forcing over the Beaufort Sea, alongshore westward ice drift, and offshore Ekman transport (Meneghello et al. 2018b). Positive correlations between upwelling and SIC anomalies in the East Siberian and Laptev Seas are presumably caused by convergent ice motion associated with the same anticyclonic atmospheric circulation (Ogi and Wallace 2007; Overland et al. 2012). Negative correlations in the Kara Sea are likely also linked with the same atmospheric circulation pattern, leading to alongshore easterly winds, coastal divergence associated with offshore Ekman

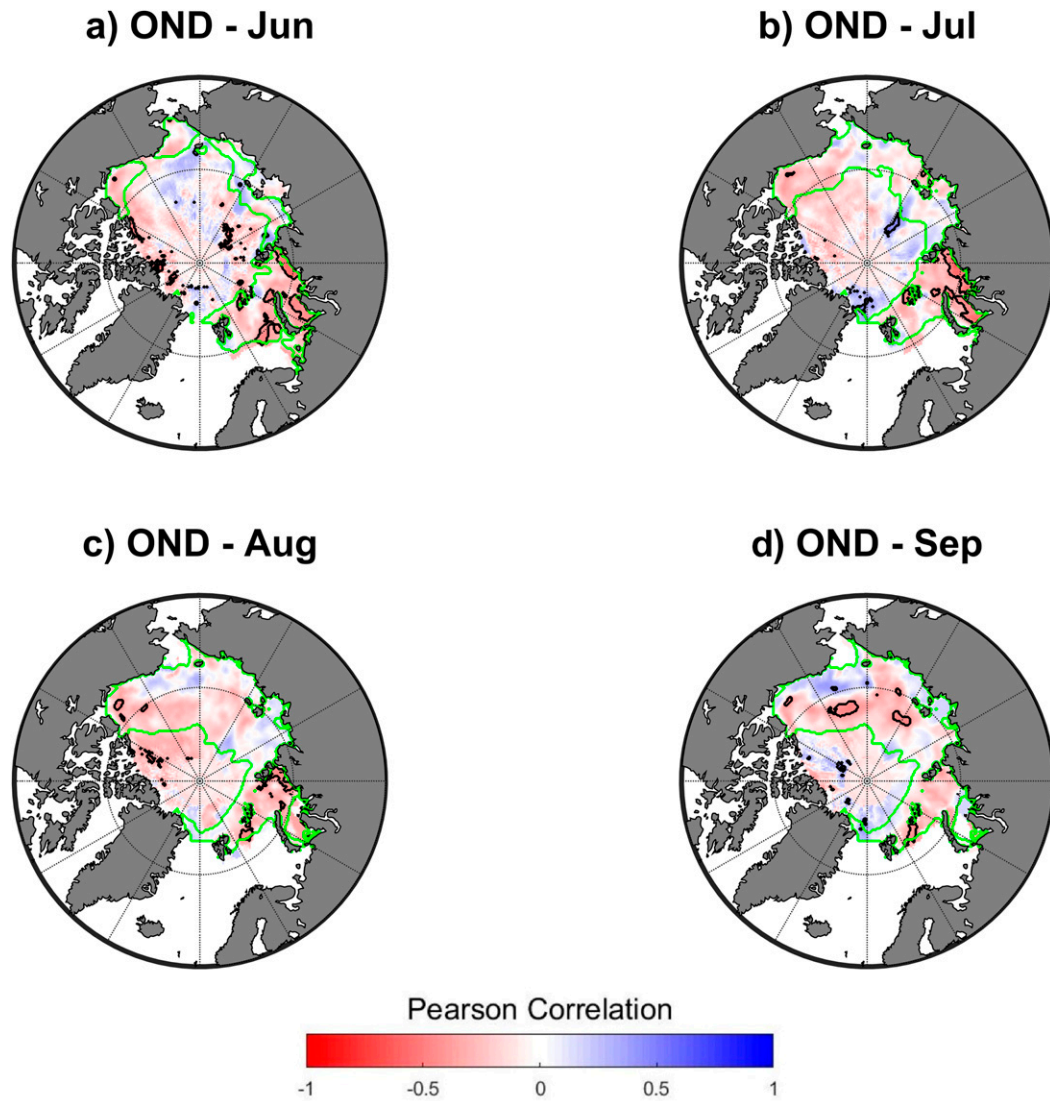


FIG. 9. Correlations between detrended ECCO October–December mean Ekman pumping velocities along the Alaskan coastline (magenta box in Fig. 1) and detrended (a) June, (b) July, (c) August, and (d) September sea ice concentration anomalies. Significant correlations (95%) are outlined in black, and regions where the interannual variability in monthly SIC varies by more than 10% are outlined in green.

transports, and negative sea ice anomalies. In the ECCO reanalysis, the strength of the tripole correlation pattern is much weaker (see Fig. 9). In this case, the correlations are more uniformly negative, especially along the Siberian coastline, with some positive correlations in the Chukchi Sea in June and in the Beaufort Sea in August and September. As for the Bering Strait OHT, discrepancies between observed and ECCO-derived time series reflect uncertainties in both records. Neither observed nor ECCO Ekman pumping anomalies are correlated with Beaufort Sea SIA on a regional scale (not shown).

Despite weak correlations between Ekman pumping and SIC at seasonal time scales, fall upwelling events have the capacity to act as a thermodynamic preconditioner for low summer sea ice concentrations. Vertical ocean heat fluxes

associated with upwelling along the Alaskan coastline have not been measured, but simulations suggest that turbulent vertical (upward) heat fluxes associated with downwelling over the Canada Basin can be as large as 20 W m^{-2} (Bourgault et al. 2020; Ramudu et al. 2018). A simple order of magnitude analysis show that these fluxes, when averaged over a 3-month period (October–December), lead to ice thickness reductions of 46 cm. This estimate is very likely an underestimate however, as upwelling along the continental slope entrains water from the deeper boundary layer, as opposed to just the surface Ekman layer in the Canada Basin, bringing additional heat to the surface (Yang 2006). These calculations suggest that large upwelling events in the fall, such as those described by Pickart et al. (2009), have the capacity to produce negative thickness

TABLE 2. Predictors, correlation coefficients (R^2), and root-mean-square errors (RMSE) in millions of square kilometers for hindcasts of July Chukchi Sea SIA from 1998 to 2015. Applying a jackknife to the modeled and observed SIAs allows for the confidence interval (σ) of each model to be given; σ is the standard deviation of possible R^2 values from the jackknife analysis.

Label	Predictors	$R^2 \pm \sigma$	RMSE
M1	Linear trend	0.42 ± 0.047	0.057
M2	Linear trend + May OHT	0.77 ± 0.028	0.036
M3	Linear trend + May SST	0.52 ± 0.039	0.052
M4	Linear trend + May SIT	0.53 ± 0.052	0.052
M5	Linear trend + May SIA	0.52 ± 0.038	0.057
M6	Linear trend + May OHT + May SIT	0.71 ± 0.052	0.040

anomalies that reemerge in the spring and summer as negative SIC anomalies in the Beaufort Sea.

c. Hindcasts for July Chukchi SIA

We present the results of July Chukchi SIA predictions from 1998 to 2015, based on the linear July Chukchi SIA trend alone (M1), the linear trend together with anomalies of Bering Strait OHT (M2), Bering Strait sea surface temperatures (SST) (M3), May Chukchi Sea SIT (M4), May Chukchi Sea SIA (M5), and May SIT and OHT (M6; see Table 2 and Fig. 10). Models based on the linear trend alone (M1) take on the mathematical form $SIA_{pred} = a_1t + C$, where SIA_{pred} is the predicted Chukchi SIA and a_1 and C are coefficients determined by the linear SIA trend over the 1998–2015 period. M2–M5 can be represented mathematically by $SIA_{pred} = a_1t + b_1X_1 + C$, where b_1 is the coefficient determined by the least squares fit between July Chukchi SIA anomalies and detrended, cumulative May Bering Strait OHT, Bering Strait SST, May SIT, or May SIA anomalies (X_1). M6 takes on the mathematical form of $SIA_{pred} = a_1t + b_2X_2 + b_1X_1 + C$, where b_1 and b_2 are the least squares regression coefficients for the May OHT and May SIT anomalies respectively, and all other variables are as before. For M2–M6, we also use a leave-one-out approach, in which we remove the target year from both time series before calculating b_1 and b_2 in order to remove the influence of the target year from the least squares fit (Williams et al. 2016; Brunette et al. 2019). This approach has the influence of reducing the skill of the models presented by approximately 3%–7%, while increasing statistical robustness. For all models, we use a jackknife approach to test the influence of individual years on the performance of each model and give a confidence interval for each model.

The simple hindcast based on a linear trend alone (M1) explains 42% ($R^2 = 0.42$) of the variance in SIA in the Chukchi Sea. The statistical hindcast based on the linear trend and May Bering Strait OHT anomalies (M2) explains 77% ($R^2 = 0.77$) of July SIA variance with a root-mean-square error (RMSE) equal to 0.036 million km^2 (4.4% of Chukchi Sea regional area). We also test the predictive skill of May Bering Strait SSTs (M3), a satellite-derived proxy for Bering Strait OHT. May Bering Strait SSTs along with the linear trend skillfully explain 52% of July SIA variance and a RMSE of 0.052 million km^2 (6.3% of Chukchi Sea area). The difference in predictive skill between Bering Strait OHT and SST anomalies is

likely due to differences between Bering Strait water temperatures and SSTs, as found by Woodgate (2018).

Next, we compare M2 and M3 with a hindcast using a linear trend and spring SIT anomalies in the Chukchi Sea (M4), a key parameter for skillful forecasts of summer Chukchi sea ice in Bushuk et al. (2017). Hindcasts utilizing May mean Chukchi SIT anomalies (M4) predict July SIA in the Chukchi Sea with $RMSE = 0.052$ million km^2 (6.3% of Chukchi Sea area) and explain 53% of Chukchi SIA variance. Hindcasts using May SIA anomalies (M5) explain a similar amount of variance as M4. Thus the use of May Bering Strait OHT in hindcasts improves predictions of July SIA in the Chukchi Sea by 35% compared to those based only on the linear trend only; and by 24% compared to those using spring SIT anomalies and the linear trend as predictors. Additionally, predictive skill from both OHT and SIT (M6) does not exceed the skill of previous models, suggesting that there is minimal predictive skill in May SIT anomalies that are not captured by May OHT anomalies. These hindcasts confirm the larger influence of the Bering Strait OHT on the interannual variability of SIA in the Chukchi Sea from May to July, and highlights the importance

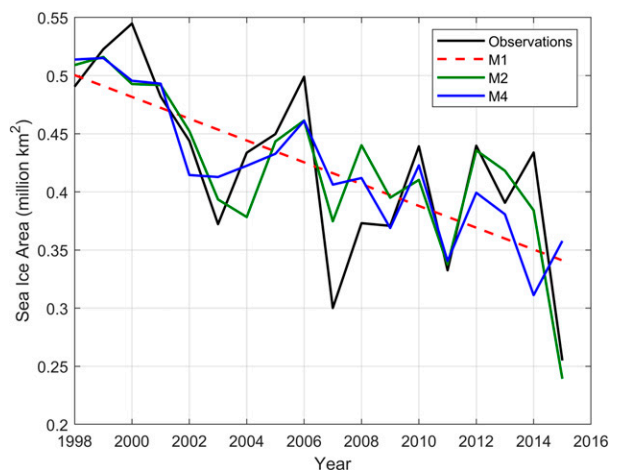


FIG. 10. Statistical hindcasts of the July SIA in the Chukchi Sea for the 1998–2015 time period and observed SIAs (black): linear trend (M1; red), linear trend + detrended, cumulative, May Bering Strait OHT anomalies (M2; green), and linear trend + mean, detrended May SIT anomalies (M4; blue). See Table 2 for hindcast statistics.

of considering Bering Strait OHT for a skillful subseasonal forecast of Chukchi SIA.

4. Conclusions

We investigate the role of Bering Strait OHT and Ekman pumping along the Alaskan coastline on the subseasonal predictability of sea ice area in the Arctic. Results show that ocean heat from the Bering Strait OHT has the largest influence on sea ice conditions in the spring and early summer in the Chukchi Sea, causing an early opening of the pack ice, a signal that is amplified by the ice-albedo feedback. Bering Strait OHT anomalies lose predictive skill in the late melt season, due to summer stratification of Chukchi Sea waters, the ice-albedo feedback, and dynamic sea ice area change associated with wind-induced sea ice drift, before reemerging in November as a delayed or early freeze onset. These findings provide observational evidence in support of a predictability gap in the Chukchi Sea, also seen in seasonal forecast studies based on fully coupled models such as Bushuk et al. (2017). Additionally, decomposition of Bering Strait OHT components (volume transports and water temperatures) shows that predictive skill is primarily derived from water temperature anomalies and not volume transport anomalies. We also document a link between Bering Strait OHT anomalies and sea ice conditions in the Atlantic sector of the Arctic, with larger than normal sea ice concentrations for positive Bering Strait OHT anomalies, potentially attributable to an anticorrelation between volume flux through Bering Strait and the Barents Sea Opening and Fram Strait.

Ekman upwelling velocity anomalies along the Alaskan continental shelf (a proxy for vertical ocean heat transport) provide no seasonal sea ice area predictability at regional or local scales. We instead find that correlations between Ekman velocities and sea ice concentration are due to dynamic sea ice motion associated with an upwelling-favorable atmospheric circulation. This anticyclonic circulation pattern leads to coastal divergence and sea ice export from the Beaufort Sea and sea ice convergence along the Siberian coastline. We however also present a simple order of magnitude analysis, which shows that large fall upwelling events, despite minimal predictive skill, have the capacity to limit fall sea ice growth and act as a thermodynamic preconditioner for spring and summer sea ice conditions.

We also present the results from six hindcasts based on the linear trend and Bering Strait OHT, SST, SIT, and SIA anomalies at the onset of melt season. Results show that including Bering Strait OHT or SIT anomalies as predictors improve hindcasts of July sea ice conditions in the Chukchi Sea with respect to a linear-trend based forecast. While SIT anomalies lead to skillful predictions of sea ice conditions in the Pacific sector (Bushuk et al. 2017), sea ice area predictability from the Bering Strait OHT exceeds that of SIT anomalies in the Chukchi Sea. Improved seasonal sea ice predictions will help increase the navigability of Arctic Ocean waters for all Arctic stakeholders.

Acknowledgments. Support for this work was provided by the National Science Foundation (NSF) Office of Polar Programs

Grant 1603914. This research is a contribution to the Forecasting Regional Arctic Sea Ice from a Month to Seasons (FRAMS) project, funded by the Marine Environmental Observation, Prediction and Response Network (MEOPAR), the National Science and Engineering Research Council (NSERC) Discovery Program, the Canadian Sea Ice and Snow Evolution Network (CanSISE), funded by NSERC Climate Change and Atmospheric Research Program, and the NSF Office of Polar Program Grants 1504023 and 1603350. Jed Lenetsky is grateful for funding received through an Undergraduate Research Award from the NSERC of Canada and Fonds de Recherche du Québec–Nature et Technologie (FRONT). Charles Brunette wishes to thank FRONT, ArcTrain, Québec-Océan, and McGill University for their support. Gianluca Meneghello received funding from the NSF Office of Polar Programs, Grant 1603557.

Data availability statement. Bering Strait mooring data are available from the University of Washington, Seattle (<http://psc.apl.washington.edu/HLD/>) and Ekman pumping fields are available at <http://mgl.mit.edu/data/weeklyEkmanPumping.nc>. Sea ice concentration fields are available at <https://nsidc.org/data/NSIDC-0051/versions/1>, PIOMAS ice thickness fields are available at <http://psc.apl.uw.edu/research/projects/arctic-sea-ice-volume-anomaly/data/>, and SST fields are available at <https://psl.noaa.gov/data/gridded/data.noaa.oisst.v2.highres.html>. We would like to thank our anonymous reviewers for their constructive feedback.

REFERENCES

- Armitage, T. W. K., S. Bacon, A. L. Ridout, S. F. Thomas, Y. Aksenov, and D. J. Wingham, 2016: Arctic sea surface height variability and change from satellite radar altimetry and GRACE, 2003–2014. *J. Geophys. Res. Oceans*, **121**, 4303–4322, <https://doi.org/10.1002/2015JC011579>.
- , —, —, A. A. Petty, S. Wolbach, and M. Tsamados, 2017: Arctic Ocean surface geostrophic circulation 2003–2014. *Cryosphere*, **11**, 1767–1780, <https://doi.org/10.5194/tc-11-1767-2017>.
- Armstrong, A., L.-B. Tremblay, and L. Mysak, 2003: A data–model intercomparison study of Arctic sea-ice variability. *Climate Dyn.*, **20**, 465–476, <https://doi.org/10.1007/s00382-002-0284-2>.
- Auclair, G., and L. Tremblay, 2018: The role of ocean heat transport in rapid sea ice declines in the Community Earth System model large ensemble. *J. Geophys. Res. Oceans*, **123**, 8941–8957, <https://doi.org/10.1029/2018JC014525>.
- Babb, D. G., R. J. Galley, D. G. Barber, and S. Rysgaard, 2016: Physical processes contributing to an ice free Beaufort Sea during September 2012. *J. Geophys. Res. Oceans*, **121**, 267–283, <https://doi.org/10.1002/2015JC010756>.
- Blanchard-Wrigglesworth, E., and M. Bushuk, 2019: Robustness of Arctic sea-ice predictability in GCMs. *Climate Dyn.*, **52**, 5555–5566, <https://doi.org/10.1007/s00382-018-4461-3>.
- , K. C. Armour, C. M. Bitz, and E. DeWeaver, 2011: Persistence and inherent predictability of Arctic sea ice in a GCM ensemble and observations. *J. Climate*, **24**, 231–250, <https://doi.org/10.1175/2010JCLI3775.1>.
- , and Coauthors, 2017: Multi-model seasonal forecast of Arctic sea-ice: Forecast uncertainty at pan-Arctic and regional scales. *Climate Dyn.*, **49**, 1399–1410, <https://doi.org/10.1007/s00382-016-3388-9>.

- Boer, A. M., E. Gavilan Pascual-Ahuir, D. P. Stevens, L. Chafik, D. K. Hutchinson, Q. Zhang, L. C. Sime, and A. J. Willmott, 2018: Interconnectivity between volume transports through Arctic straits. *J. Geophys. Res. Oceans*, **123**, 8714–8729, <https://doi.org/10.1029/2018JC014320>.
- Bonan, D. B., M. Bushuk, and M. Winton, 2019: A spring barrier for regional predictions of summer Arctic sea ice. *Geophys. Res. Lett.*, **46**, 5937–5947, <https://doi.org/10.1029/2019GL082947>.
- Bourgault, P., D. Straub, K. Duquette, L.-P. Nadeau, and B. Tremblay, 2020: Vertical heat fluxes beneath idealized sea ice leads in large-eddy simulations: Comparison with observations from the SHEBA experiment. *J. Phys. Oceanogr.*, **50**, 2189–2202, <https://doi.org/10.1175/JPO-D-19-0298.1>.
- Brunette, C., B. Tremblay, and R. Newton, 2019: Winter coastal divergence as a predictor for the minimum sea ice extent in the Laptev Sea. *J. Climate*, **32**, 1063–1080, <https://doi.org/10.1175/JCLI-D-18-0169.1>.
- Bushuk, M., R. Msadek, M. Winton, G. Vecchi, R. Gudgel, A. Rosati, and X. Yang, 2017: Skillful regional prediction of Arctic sea ice on seasonal timescales. *Geophys. Res. Lett.*, **44**, 4953–4964, <https://doi.org/10.1002/2017GL073155>.
- Cavaleri, D. J., C. L. Parkinson, P. Gloersen, and H. J. Zwally, 1996: Sea ice concentrations from Nimbus-7 SMMR and DMSP SSM/ISSMIS passive microwave data. 1978–2007, National Snow and Ice Data Center, accessed 2017, <https://doi.org/10.5067/8GQ8LZQVL0VL>.
- Chevallier, M., D. Salas y Melia, A. Voldoire, M. Deque, and G. Garric, 2013: Seasonal forecasts of the pan-Arctic sea ice extent using a GCM-based seasonal prediction system. *J. Climate*, **26**, 6092–6104, <https://doi.org/10.1175/JCLI-D-12-00612.1>.
- Danielson, S. L., T. J. Weingartner, K. S. Hedstrom, K. Aagaard, R. Woodgate, E. Curchitser, and P. J. Stabeno, 2014: Coupled wind-forced controls of the Bering–Chukchi shelf circulation and the Bering Strait throughflow: Ekman transport, continental shelf waves, and variations of the Pacific–Arctic sea surface height gradient. *Prog. Oceanogr.*, **125**, 40–61, <https://doi.org/10.1016/j.pocean.2014.04.006>.
- Day, J., S. Tietsche, and E. Hawkins, 2014: Pan-Arctic and regional sea ice predictability: Initialization month dependence. *J. Climate*, **27**, 4371–4390, <https://doi.org/10.1175/JCLI-D-13-00614.1>.
- Dmitrenko, I. A., and Coauthors, 2018: Wind-forced depth-dependent currents over the eastern Beaufort Sea continental slope: Implications for Pacific water transport. *Elementa*, **6**, 66, <https://doi.org/10.1525/elementa.321>.
- ECCO Consortium, I. Fukumori, O. Wang, I. Fenty, G. Forget, P. Heimbach, and R. M. Ponte, 2020a: ECCO central estimate (version 4 release 4), <https://ecco.jpl.nasa.gov/drive/files/Version5>.
- , —, —, —, —, and —, 2020b: Synopsi of the ECCO central production global ocean and sea-ice state estimate. Tech. Rep., 17 pp., <https://zenodo.org/record/3765929>.
- Forget, G., J.-M. Campin, P. Heimbach, C. N. Hill, R. M. Ponte, and C. Wunsch, 2015: ECCO version 4: An integrated framework for non-linear inverse modeling and global ocean state estimation. *Geosci. Model Dev.*, **8**, 3071–3104, <https://doi.org/10.5194/gmd-8-3071-2015>.
- Foukal, N. P., R. S. Pickart, G. W. K. Moore, and P. Lin, 2019: Shelfbreak downwelling in the Alaskan Beaufort Sea. *J. Geophys. Res. Oceans*, **124**, 7201–7225, <https://doi.org/10.1029/2019JC015520>.
- Gong, D., and R. S. Pickart, 2015: Summertime circulation in the eastern Chukchi Sea. *Deep-Sea Res. II*, **118**, 18–31, <https://doi.org/10.1016/j.dsr2.2015.02.006>.
- Guemas, V., M. Chevallier, M. Déqué, O. Bellprat, and F. Doblas-Reyes, 2016: Impact of sea ice initialization on sea ice and atmosphere prediction skill on seasonal timescales. *Geophys. Res. Lett.*, **43**, 3889–3896, <https://doi.org/10.1002/2015GL066626>.
- Jahn, A., L. B. Tremblay, R. Newton, M. M. Holland, L. A. Mysak, and I. A. Dmitrenko, 2010: A tracer study of the Arctic Ocean’s liquid freshwater export variability. *J. Geophys. Res. Oceans*, **115**, C07015, <https://doi.org/10.1029/2009JC005873>.
- Kalnay, E., and Coauthors, 1996: The NCEP/NCAR 40-Year Reanalysis Project. *Bull. Amer. Meteor. Soc.*, **77**, 437–471, [https://doi.org/10.1175/1520-0477\(1996\)077<0437:TNYRP>2.0.CO;2](https://doi.org/10.1175/1520-0477(1996)077<0437:TNYRP>2.0.CO;2).
- Lei, R., D. Gui, P. Heil, J. K. Hutchings, and M. Ding, 2020: Comparisons of sea ice motion and deformation, and their responses to ice conditions and cyclonic activity in the western Arctic Ocean between two summers. *Cold Reg. Sci. Technol.*, **170**, 102925, <https://doi.org/10.1016/j.coldregions.2019.102925>.
- Lin, P., R. S. Pickart, K. M. Stafford, G. W. K. Moore, D. J. Torres, F. Bahr, and J. Hu, 2016: Seasonal variation of the Beaufort shelfbreak jet and its relationship to Arctic cetacean occurrence. *J. Geophys. Res. Oceans*, **121**, 8434–8454, <https://doi.org/10.1002/2016JC011890>.
- , —, G. W. K. Moore, M. A. Spall, and J. Hu, 2019: Characteristics and dynamics of wind-driven upwelling in the Alaskan Beaufort Sea based on six years of mooring data. *Deep-Sea Res. II*, **162**, 79–92, <https://doi.org/10.1016/j.dsr2.2018.01.002>.
- Lu, K., S. Danielson, K. Hedstrom, and T. Weingartner, 2020: Assessing the role of oceanic heat fluxes on ice ablation of the central Chukchi Sea Shelf. *Prog. Oceanogr.*, **184**, 102313, <https://doi.org/10.1016/j.pocean.2020.102313>.
- Meier, W. N., F. Fetterer, M. Savoie, S. Mallory, R. Duerr, and J. Stroeve, 2017: NOAA/NSIDC climate data record of passive microwave sea ice concentration, version 3. National Snow and Ice Data Center, accessed 2019, <https://doi.org/10.7265/N59P2ZTG>.
- Meneghello, G., J. Marshall, J.-M. Campin, E. Doddridge, and M.-L. Timmermans, 2018a: The ice-ocean governor: Ice-ocean stress feedback limits Beaufort Gyre spin-up. *Geophys. Res. Lett.*, **45**, 11 293–11 299, <https://doi.org/10.1029/2018GL080171>.
- , —, M.-L. Timmermans, and J. Scott, 2018b: Observations of seasonal upwelling and downwelling in the Beaufort Sea mediated by sea ice. *J. Phys. Oceanogr.*, **48**, 795–805, <https://doi.org/10.1175/JPO-D-17-0188.1>.
- Ogi, M., and J. M. Wallace, 2007: Summer minimum Arctic sea ice extent and the associated summer atmospheric circulation. *Geophys. Res. Lett.*, **34**, L12705, <https://doi.org/10.1029/2007GL029897>.
- Okkonen, S. R., C. J. Ashjian, R. G. Campbell, W. Maslowski, J. L. Clement-Kinney, and R. Potter, 2009: Intrusion of warm Bering/Chukchi waters onto the shelf in the western Beaufort Sea. *J. Geophys. Res.*, **114**, C00A11, <https://doi.org/10.1029/2008JC004870>.
- Overland, J. E., J. A. Francis, E. Hanna, and M. Wang, 2012: The recent shift in early summer Arctic atmospheric circulation. *Geophys. Res. Lett.*, **39**, L19804, <https://doi.org/10.1029/2012GL053268>.
- Parkinson, C. L., 2014: Spatially mapped reductions in the length of the Arctic Sea ice season. *Geophys. Res. Lett.*, **41**, 4316–4322, <https://doi.org/10.1002/2014GL060434>.
- Pearce, T., J. Ford, A. C. Willox, and B. Smit, 2015: Inuit Traditional Ecological Knowledge (TEK), subsistence hunting and adaptation to climate change in the Canadian Arctic. *Arctic*, **68**, 233–245, <https://doi.org/10.14430/arctic4475>.
- Peng, G., W. Meier, D. Scott, and M. Savoie, 2013: A long-term and reproducible passive microwave sea ice concentration data

- record for climate studies and monitoring. *Earth Syst. Sci. Data*, **5**, 311–318, <https://doi.org/10.5194/essd-5-311-2013>.
- Peralta-Ferriz, C., and R. A. Woodgate, 2017: The dominant role of the East Siberian Sea in driving the oceanic flow through the Bering Strait—Conclusions from GRACE ocean mass satellite data and in situ mooring observations between 2002 and 2016. *Geophys. Res. Lett.*, **44**, 11 472–11 481, <https://doi.org/10.1002/2017GL075179>.
- Perovich, D., B. Light, H. Eicken, K. Jones, K. Runciman, and S. Nghiem, 2007: Increasing solar heating of the Arctic Ocean and adjacent seas, 1979–2005: Attribution and role in the ice-albedo feedback. *Geophys. Res. Lett.*, **34**, L19505, <https://doi.org/10.1029/2007GL031480>.
- Pickart, R. S., G. W. K. Moore, D. J. Torres, P. S. Fratantoni, R. A. Goldsmith, and J. Yang, 2009: Upwelling on the continental slope of the Alaskan Beaufort Sea: Storms, ice, and oceanographic response. *J. Geophys. Res.*, **114**, C00A13, <https://doi.org/10.1029/2008JC005009>.
- , —, C. Mao, F. Bahr, C. Nobre, and T. J. Weingartner, 2016: Circulation of winter water on the Chukchi shelf in early summer. *Deep-Sea Res. II*, **130**, 56–75, <https://doi.org/10.1016/j.jdsr.2016.05.001>.
- Ramudu, E., R. Gelderloos, D. Yang, C. Meneveau, and A. Gnanadesikan, 2018: Large eddy simulation of heat entrainment under Arctic sea ice. *J. Geophys. Res. Oceans*, **123**, 287–304, <https://doi.org/10.1002/2017JC013267>.
- Schreiber, E. A. P., and M. C. Serreze, 2020: Impacts of synoptic-scale cyclones on Arctic sea-ice concentration: A systematic analysis. *Ann. Glaciol.*, **61**, 139–153, <https://doi.org/10.1017/aog.2020.23>.
- Schweiger, A., R. Lindsay, J. Zhang, M. Steele, H. Stern, and R. Kwok, 2011: Uncertainty in modeled Arctic sea ice volume. *J. Geophys. Res.*, **116**, C00D06, <https://doi.org/10.1029/2011JC007084>.
- Serreze, M. C., A. D. Crawford, J. C. Stroeve, A. P. Barrett, and R. A. Woodgate, 2016: Variability, trends, and predictability of seasonal sea ice retreat and advance in the Chukchi Sea. *J. Geophys. Res. Oceans*, **121**, 7308–7325, <https://doi.org/10.1002/2016JC011977>.
- , A. P. Barrett, A. D. Crawford, and R. A. Woodgate, 2019: Monthly variability in Bering strait oceanic volume and heat transports, links to atmospheric circulation and ocean temperature, and implications for sea ice conditions. *J. Geophys. Res. Oceans*, **124**, 9317–9337, <https://doi.org/10.1029/2019JC015422>.
- Sigmond, M., M. C. Reader, G. M. Flato, W. J. Merryfield, and A. Tivy, 2016: Skillful seasonal forecasts of Arctic sea ice retreat and advance dates in a dynamical forecast system. *Geophys. Res. Lett.*, **43**, 12 457–12 465, <https://doi.org/10.1002/2016GL071396>.
- Spall, M. A., R. S. Pickart, M. Li, M. Itoh, P. Lin, T. Kikuchi, and Y. Qi, 2018: Transport of Pacific water into the Canada Basin and the formation of the Chukchi Slope Current. *J. Geophys. Res. Oceans*, **123**, 7453–7471, <https://doi.org/10.1029/2018JC013825>.
- Steele, M., J. Morison, W. Ermold, I. Rigor, M. Ortmeier, and K. Shimada, 2004: Circulation of summer Pacific halocline water in the Arctic Ocean. *J. Geophys. Res.*, **109**, C02027, <https://doi.org/10.1029/2003JC002009>.
- Stigebrandt, A., 1981: A model for the thickness and salinity of the upper layer in the Arctic Ocean and the relationship between the ice thickness and some external parameters. *J. Phys. Oceanogr.*, **11**, 1407–1422, [https://doi.org/10.1175/1520-0485\(1981\)011<1407:AMFTTA>2.0.CO;2](https://doi.org/10.1175/1520-0485(1981)011<1407:AMFTTA>2.0.CO;2).
- Tandon, N. F., P. J. Kushner, D. Docquier, J. J. Wettstein, and C. Li, 2018: Reassessing sea ice drift and its relationship to long-term Arctic sea ice loss in coupled climate models. *J. Geophys. Res. Oceans*, **123**, 4338–4359, <https://doi.org/10.1029/2017JC013697>.
- Tietsche, S., and Coauthors, 2014: Seasonal to interannual Arctic sea ice predictability in current global climate models. *Geophys. Res. Lett.*, **41**, 1035–1043, <https://doi.org/10.1002/2013GL058755>.
- Timmermans, M.-L., and J. Marshall, 2020: Understanding Arctic Ocean circulation: A review of ocean dynamics in a changing climate. *J. Geophys. Res. Oceans*, **125**, e2018JC014378, <https://doi.org/10.1029/2018JC014378>.
- , and Coauthors, 2014: Mechanisms of Pacific summer water variability in the Arctic's Central Canada Basin. *J. Geophys. Res. Oceans*, **119**, 7523–7548, <https://doi.org/10.1002/2014JC010273>.
- Toole, J. M., M.-L. Timmermans, D. K. Perovich, R. A. Krishfield, A. Proshutinsky, and J. A. Richter-Menge, 2010: Influences of the ocean surface mixed layer and thermohaline stratification on Arctic sea ice in the central Canada Basin. *J. Geophys. Res.*, **115**, C10018, <https://doi.org/10.1029/2009JC005660>.
- Tschudi, M., C. Fowler, J. Stewart, and W. N. Meier, 2016: Polar pathfinder daily 25 km EASE-Grid sea ice motion vectors, version 3. NASA National Snow and Ice Data Center Distributed Active Archive Center, accessed 2017, <https://doi.org/10.5067/O57VAIT2AYYY>.
- United States Navy, 2014: The United States Navy Arctic Roadmap for 2014 to 2030. Tech. Rep., Department of the Navy, Washington, DC, 38 pp., www.navy.mil/docs/USN_arctic_roadmap.pdf.
- von Appen, W.-J., and R. S. Pickart, 2012: Two configurations of the Western Arctic Shelfbreak Current in summer. *J. Phys. Oceanogr.*, **42**, 329–351, <https://doi.org/10.1175/JPO-D-11-026.1>.
- Williams, J., B. Tremblay, R. Newton, and R. Allard, 2016: Dynamic preconditioning of the minimum September sea-ice extent. *J. Climate*, **29**, 5879–5891, <https://doi.org/10.1175/JCLI-D-15-0515.1>.
- Woodgate, R., 2018: Increases in the Pacific inflow to the Arctic from 1990 to 2015, and insights into seasonal trends and driving mechanisms from year-round Bering Strait mooring data. *Prog. Oceanogr.*, **160**, 124–154, <https://doi.org/10.1016/j.pocean.2017.12.007>.
- , T. Weingartner, and R. Lindsay, 2010: The 2007 Bering Strait oceanic heat flux and anomalous Arctic sea-ice retreat. *Geophys. Res. Lett.*, **37**, L01602, <https://doi.org/10.1029/2009GL041621>.
- , K. Stafford, and F. Prah, 2015: A synthesis of year-round interdisciplinary mooring measurements in the Bering Strait (1990–2014) and the RUSALCA years (2004–2011). *Oceanography*, **28**, 46–67, <https://doi.org/10.5670/oceanog.2015.57>.
- Yang, J., 2006: The seasonal variability of the Arctic Ocean Ekman transport and its role in the mixed layer heat and salt fluxes. *J. Climate*, **19**, 5366–5387, <https://doi.org/10.1175/JCLI3892.1>.
- Zhang, J., and D. A. Rothrock, 2003: Modeling global sea ice with a thickness and enthalpy distribution model in generalized curvilinear coordinates. *Mon. Wea. Rev.*, **131**, 845–861, [https://doi.org/10.1175/1520-0493\(2003\)131<0845:MGSIWA>2.0.CO;2](https://doi.org/10.1175/1520-0493(2003)131<0845:MGSIWA>2.0.CO;2).
- , R. Lindsay, A. Schweiger, and M. Steele, 2013: The impact of an intense summer cyclone on 2012 Arctic sea ice retreat. *Geophys. Res. Lett.*, **40**, 720–726, <https://doi.org/10.1002/grl.50190>.